LETTER

doi:10.1038/nature20114

Emergence of a turbulent cascade in a quantum gas

Nir Navon[1], Alexander L. Gaunt[1], Robert P. Smith[1] & Zoran Hadzibabic[1]

A central concept in the modern understanding of turbulence is the existence of cascades of excitations from large to small length scales, or vice versa. This concept was introduced in 1941 by Kolmogorov and Obukhov[1,2], and such cascades have since been observed in various systems, including interplanetary plasmas[3], supernovae[4], ocean waves[5] and financial markets[6]. Despite much progress, a quantitative understanding of turbulence remains a challenge, owing to the interplay between many length scales that makes theoretical simulations of realistic experimental conditions difficult. Here we observe the emergence of a turbulent cascade in a weakly interacting homogeneous Bose gas—a quantum fluid that can be theoretically described on all relevant length scales. We prepare a Bose–Einstein condensate in an optical box[7], drive it out of equilibrium with an oscillating force that pumps energy into the system at the largest length scale, study its nonlinear response to the periodic drive, and observe a gradual development of a cascade characterized by an isotropic power-law distribution in momentum space. We numerically model our experiments using the Gross–Pitaevskii equation and find excellent agreement with the measurements. Our experiments establish the uniform Bose gas as a promising new medium for investigating many aspects of turbulence, including the interplay between vortex and wave turbulence, and the relative importance of quantum and classical effects.

Compared to classical fluids, superfluids present fascinating peculiarities such as irrotational and frictionless flow, which raises fundamental questions about the character of turbulent cascades[8,9]. Numerous experiments on quantum-fluid turbulence have been performed with liquid helium, exploring both vortex[8,10–12] and wave turbulence[13–15], but their theoretical understanding is hampered by the strong interactions that make first-principles descriptions intractable. The situation is *a priori* simpler for an ultracold, weakly interacting Bose gas, which is often accurately described by the Gross–Pitaevskii equation (GPE) for the complex-valued matter field $\psi(\boldsymbol{r}, t)$ (where $\boldsymbol{r} = (x, y, z)$ is the spatial position and t is time; ref. 16). This equation is widely used to model turbulence in quantum fluids[17–21], but the numerical results have been lacking experimental validation. Experimentally, qualitative evidence for turbulence has been seen in quantum gases[22–25], but quantitative comparisons with theory were hindered by the inhomogeneous density that results from harmonic trapping. Here we eliminate this problem by studying turbulence in a homogeneous quantum gas.

The basic idea of our experiment is outlined in Fig. 1. We prepare a quasi-pure Bose–Einstein condensate (BEC) of ^{87}Rb atoms in a cylindrical optical box[7], and drive it out of equilibrium with a spatially uniform, oscillating force that primarily couples to the lowest, dipole-like axial mode. Our box has length $L = 27(1)\,\mu$m and radius $R = 16(1)\,\mu$m (here and elsewhere, errors represent 1σ uncertainties). For our typical atom number $N \approx 10^5$, the initial, equilibrium BEC has a chemical potential $\mu/k_B \approx 2$ nK (where k_B is the Boltzmann constant), interaction energy per particle $E_{int}/k_B \approx 1$ nK and negligible kinetic energy, while the critical temperature for Bose–Einstein condensation is $T_c \approx 50$ nK. The driving force is provided by a magnetic field gradient that creates a potential $U(\boldsymbol{r}) = \Delta U z/L$, where the coordinate z is along the axis of the box (Fig. 1a). The natural scale for ΔU, separating weak and strong drives, is set by μ.

Numerical simulations in Fig. 1a show the microscopic behaviour of a shaken trapped gas, which gradually changes from simple unidirectional sloshing along z to an omnidirectional turbulent flow; in addition to the wave-like motion, we observe vortex lines (depicted in red), which are detected by computing the local circulation. (Snapshots of the turbulent flow do not obey the cylindrical symmetry of the (time-dependent) Hamiltonian. In real physical systems, any such symmetry is always broken by imperfections; in our simulations the symmetry breaking is provided by the position of the numerical grid.) Here the shaking amplitude is $\Delta U/\mu = 1$ and the longest shaking time $t_s = 2$ s corresponds to 16 driving periods.

Experimentally, we probe the global properties of the gas by releasing it from the trap and imaging it along a radial direction (x) after a long

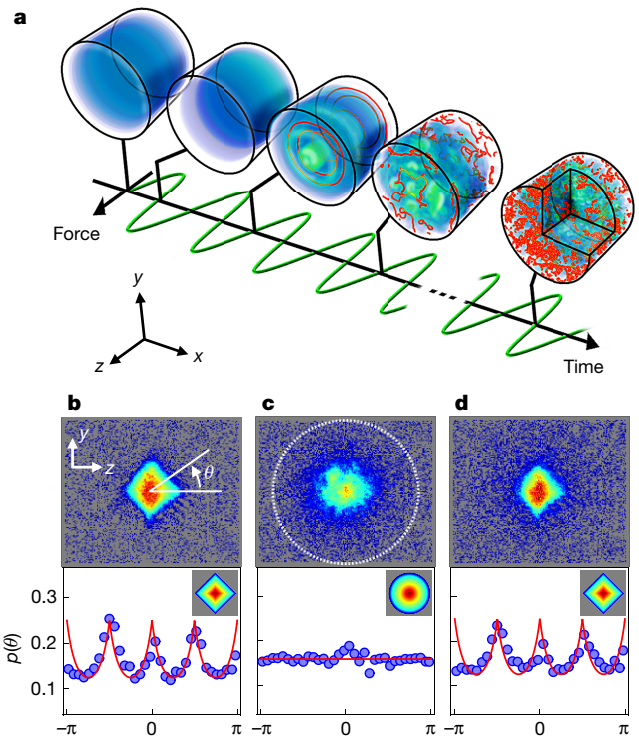

Figure 1 | From unidirectional sloshing to isotropic turbulence. **a**, Gross–Pitaevskii simulations of a shaken, box-trapped Bose gas. The blue shading indicates the gas density; the red lines indicate vortices. **b**–**d**, Experimental absorption images taken along x after 100 ms of TOF expansion, with $N \approx 8 \times 10^4$ atoms (upper panels), and the corresponding angular distributions $p(\theta)$, averaged over 20 images taken under identical conditions (lower panels). **b**, Initial BEC; **c**, after shaking for 2 s at 8 Hz with amplitude $\Delta U/\mu \approx 1.2$; and **d**, after the turbulent cloud was allowed to relax for 1.5 s. The dashed circle in **c** corresponds to an expansion energy of $k_B T_c/2$. In the lower panels, the red lines correspond to the diamond-like and isotropic distributions depicted in the insets.

[1]Cavendish Laboratory, University of Cambridge, J. J. Thomson Avenue, Cambridge CB3 0HE, UK.

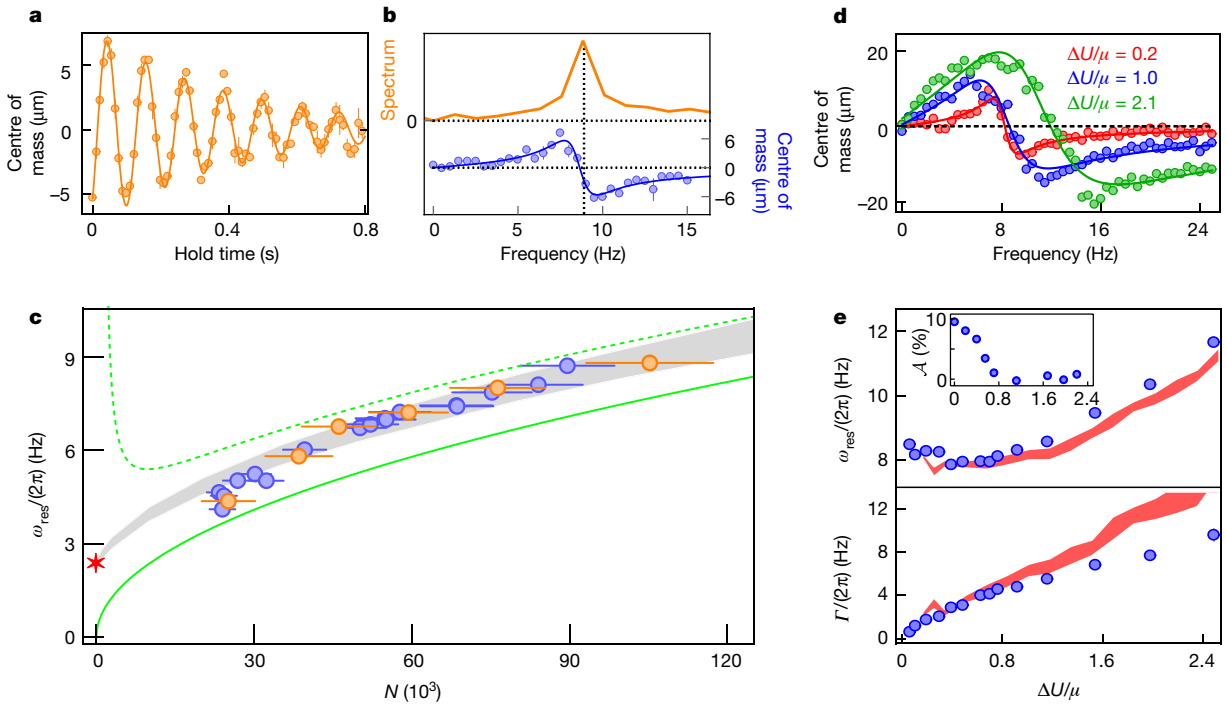

Figure 2 | Nonlinear spectroscopy of the lowest axial mode of the BEC and the route to turbulence. a, **b**, Small-amplitude oscillations of the centre of mass (along the z axis, see Fig. 1a) for $N = 10(1) \times 10^4$. **a**, Free oscillation after a 20-ms kick with $\Delta U/k_B = 1.7$ nK. **b**, Fourier spectrum of the free oscillation in **a** (orange line), and displacement after a whole number of driven oscillations, with driving amplitude $\Delta U/k_B = 0.3$ nK and $t_s = 2$ s (blue points). The solid blue line is a fit (see Methods). Error bars in **a** and **b** represent 1σ errors. **c**, Small-amplitude ω_{res} versus N for free (orange) and driven (blue) oscillations with the same ΔU and t_s values as in **a** and **b**. Horizontal error bars represent 1σ errors; the ω_{res} errors are smaller than the point size. The grey shaded area shows numerical solutions of the Bogoliubov equations and the red star is the analytical non-interacting limit. Green lines are based on hydrodynamic approximations (see text). **d**, **e**, Nonlinear response, for $N = 8(1) \times 10^4$. **d**, Driven-oscillation signals as in **b**, for various ΔU. **e**, ω_{res} and linewidth Γ versus ΔU (blue points), and the corresponding results of GPE simulations (red bands). Inset, TOF anisotropy $\mathcal{A}$ versus $\Delta U/\mu$ for $t_s = 4$ s of resonant driving. All measurements of the centre of mass were done with $t_{TOF} = 140$ ms.

time-of-flight (TOF) expansion, $t_{TOF} \geq 100$ ms. From the images we extract the centre of mass and momentum distribution of the cloud. The position of the centre of mass reflects the axial in-trap sloshing, and the evolution of the momentum distribution reveals the cascade of excitations from small to large wavevectors $\boldsymbol{k}$—the so-called direct cascade.

In Fig. 1b–d we show a qualitative experimental signature of turbulence with three key examples of TOF images (upper panels) and the corresponding angular distributions of atoms $p(\theta)$ (lower panels). The initial BEC (Fig. 1b) shows an anisotropic expansion, which is driven by the conversion of interaction into kinetic energy, and reflects the shape of the container[26]. In sharp contrast, after sufficiently long shaking the expansion is isotropic (Fig. 1c), with $p(\theta)$ exhibiting small fluctuations around $1/(2\pi)$. This is the first qualitative signature of a kinetic-energy-dominated turbulent state, in which the long-range coherence of the BEC is destroyed. We stress that this highly non-equilibrium state is fundamentally different from an equilibrium non-condensed state, which is also kinetic-energy-dominated and displays isotropic expansion. The key point is that, in our box trap, there is a large separation between the initial E_{int} and $k_B T_c$. This gives us access to the regime in which the total (mostly kinetic) energy per particle E satisfies $E_{int} \ll E \ll k_B T_c$. In this regime, coherence is destroyed in the turbulent state, but the corresponding equilibrium state with the same E is still deeply condensed. In Fig. 1c, the dashed circle corresponds to an expansion energy of $k_B T_c/2$, and the average energy of the atoms is clearly much lower; from the second moment of the TOF distribution we get $E \approx 0.12 k_B T_c$, which in equilibrium would correspond to a condensed fraction $\eta \approx 0.7$ (ref. 27). Indeed, if we stop shaking and allow the turbulent gas to relax, a BEC reforms (Fig. 1d) with the expected $\eta = 0.7(1)$. For all our studies of the turbulent state we restrict the shaking amplitude ($\Delta U \lesssim 2\mu$) and time ($t_s \leq 4$ s) so that $E < 0.25 k_B T_c$, which corresponds to an equilibrium η of >0.5.

To see how pumping energy at the largest length scale (with a spatially uniform force) leads to a turbulent cascade, we perform detailed spectroscopy of the lowest-lying axial mode of the BEC (see Fig. 2). In contrast to the harmonic trap, for which the dipole mode is fixed by the trapping frequency (Kohn's theorem), in the box it depends on interactions, which results in nonlinear behaviour for non-vanishing shaking amplitudes.

We first study the small-amplitude centre-of-mass response for various N, using both free and driven oscillations. In the first method, we pulse on a constant ΔU for a short time and let the gas oscillate freely in the trap for a variable hold time before releasing it and measuring the centre of mass in TOF (Fig. 2a). In the Fourier spectrum of this oscillation (orange line in Fig. 2b) we see a single strong peak, with no indication that the gradient kick directly couples to other low-lying modes. In the second method, we apply a continuous oscillating drive of (angular) frequency ω and amplitude $\Delta U \lesssim 0.5\mu$, and perform TOF measurements after a whole number of drive periods. Similarly to a driven harmonic oscillator, the displacement of the centre of mass has a dispersive line shape as a function of ω, vanishing on resonance (see Methods). As shown in Fig. 2b, the two methods give the same resonant frequency ω_{res}.

In Fig. 2c we plot the small-amplitude ω_{res} versus N, and compare the data with various theories. The hydrodynamic prediction (solid green line) is $\omega_{HD} = \pi c/L$, where $c = \sqrt{\mu/m}$ is the speed of sound and m is the atom mass. This theory assumes that the healing length $\xi = \hbar/\sqrt{2m\mu}$ (where $\hbar$ is the reduced Planck constant) satisfies $\xi \ll L$. It is therefore not applicable in the $N \to 0$ limit, where $\omega_{res} = 3\pi^2\hbar/(2mL^2)$ (red star in Fig. 2c) is given by the splitting of the lowest axial single-particle states. For our largest BEC, $L/\xi \approx 20$, but ω_{HD} is still

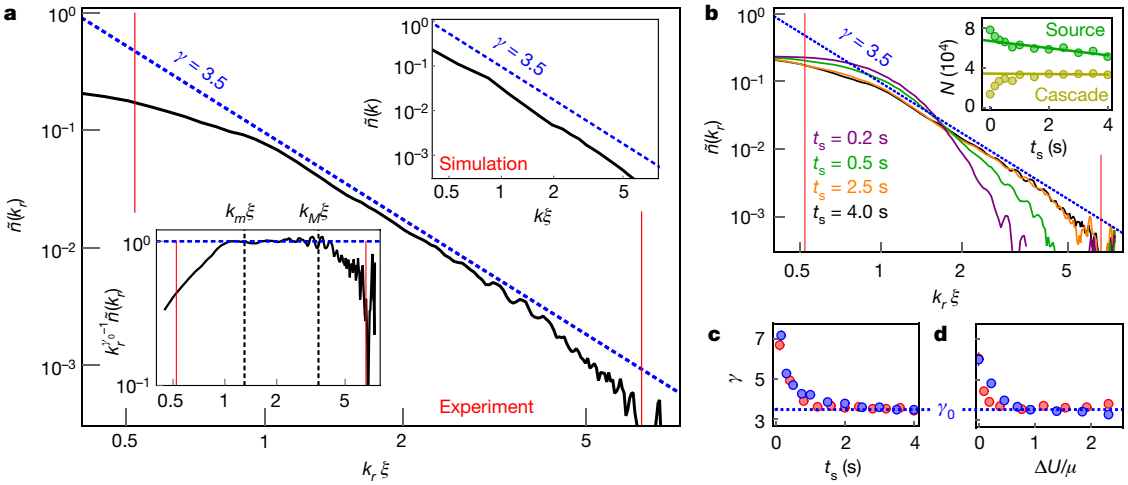

Figure 3 | Development of a turbulent cascade. a, Momentum distribution of the turbulent gas (solid black line), for $N = 7(1) \times 10^4$, $\Delta U/\mu = 1.1(1)$, $t_s = 4$ s, $\omega/(2\pi) = 9$ Hz and $t_{TOF} = 100$ ms. The vertical red lines indicate the momentum resolution k_{low} (left) and the energy sink at k_{high} (right); the dashed blue line is a guide to the eye, offset from the data for clarity. Lower inset, compensated spectrum $k_r^{\gamma_0-1}\tilde{n}(k_r)$ with $\gamma_0 = 3.5$ (in log–log scale); k_m and k_M define the fitting ranges used in **b**–**d**. Upper inset, steady-state distribution from GPE simulations, for $\Delta U/\mu = 1$. **b**, Dynamics of $\tilde{n}(k_r)$ towards the steady state, for $\Delta U/\mu = 1.1(1)$. Inset, total atom population for $k_r < k_m$ (the low-k 'source'; green), and for $k_m < k_r < k_M$ (in the cascade region; yellow). At long times (solid lines) $\dot{N}_{source} = -3.6(1.5)$ atoms ms^{-1}, whereas $\dot{N}_{cascade} = -0.2(3)$ atoms ms^{-1} is consistent with zero. All populations are corrected for losses due to the collisions with the background gas in the vacuum chamber (see Methods). **c**, Exponent γ versus shaking time in experiment (blue, $\Delta U/\mu = 1.1(1)$) and simulations (red, $\Delta U/\mu = 1$). **d**, Exponent γ versus shaking amplitude in experiment (blue) and simulations (red), for $t_s = 4$ s.

observably lower than ω_{res}. We empirically find that an upper bound on ω_{res} (dashed green line in Fig. 2c) is obtained by calculating ω_{HD} for an effective BEC volume that excludes the region within ξ of the trap walls. Finally, we linearize the GPE around the ground-state BEC solution for our box trap and numerically solve the resultant Bogoliubov equations (see Methods). These solutions are shown as the grey shaded area in Fig. 2c, which accounts for the experimental uncertainty in the box size. We find excellent agreement with the data, without any adjustable parameters.

In Fig. 2d, e we show measurements for driven oscillations with different drive strengths. Increasing ΔU shifts and broadens the resonance, and both trends are reproduced by our GPE simulations (red bands in Fig. 2e); for very large ΔU the classical-field GPE approximation may gradually break down. The line broadening, seen for any non-zero ΔU, indicates nonlinear coupling to other modes, which provides the route for the transfer of excitations into other directions and a direct cascade.

In the inset of Fig. 2e we plot the anisotropy of the TOF expansion $\mathcal{A} = (1/2)\int |p(\theta) - 1/(2\pi)| \mathrm{d}\theta$ (see Methods) for 4 s of resonant driving. For $\Delta U \gtrsim 0.8\mu$ we observe the isotropic expansion ($\mathcal{A} \approx 0$) that qualitatively signals turbulence. A key quantitative expectation for an isotropic turbulent cascade is the emergence of a steady-state power-law momentum distribution: $n(\boldsymbol{k}) \propto k^{-\gamma}$, where γ is a constant[28]. Owing to the line-of-sight integration in absorption imaging, this corresponds to an in-plane distribution $\tilde{n}(k) \propto k^{-(\gamma-1)}$.

In Fig. 3 we present our study of $\tilde{n}(k)$ observed after a resonant drive. An isotropic expansion (from an anisotropic container) necessarily means that the in-trap kinetic energy dominates over the interaction energy, which in turn means that the TOF expansion can provide an accurate measure of the in-trap momentum distribution. Specifically, defining $k_r \equiv mr/(\hbar t_{TOF})$, where r is distance from the centre of mass in TOF, $\tilde{n}(k_r)$ should closely correspond to the in-trap $\tilde{n}(k)$ (see Methods, Extended Data Fig. 1). However, this correspondence does not hold for very low momenta ($k_r \lesssim k_{low} \equiv mL/(\hbar t_{TOF})$), owing to the convolution of the TOF distribution with the initial (in-trap) cloud shape. The highest momentum in our clouds ($k_{high} \equiv \sqrt{2mU_0}/\hbar$) is set by the trap depth $U_0 \approx k_B \times 60$ nK, which corresponds to an energy sink.

In Fig. 3a we show an example of $\tilde{n}(k_r)$, for $\Delta U/\mu = 1.1(1)$ and $t_s = 4$ s (black line in the main panel and lower inset), obtained by averaging over 20 images and also performing an azimuthal average. Vertical red lines indicate the k_{low} and k_{high} boundaries. Away from these boundaries we observe a power-law behaviour, with $\gamma \approx 3.5$. This behaviour is even more visually evident in the lower inset, in which we plot $k_r^{\gamma_0-1}\tilde{n}(k_r)$, with $\gamma_0 \equiv 3.5$. In the top inset in Fig. 3a we show the result of GPE simulations (for $\Delta U/\mu = 1$), which also exhibit a power-law distribution. Moreover, the experiment and simulations are consistent with the same value of γ.

In Fig. 3b we present the evolution of $\tilde{n}(k_r)$ towards the turbulent steady state, as the shaking time is increased. In the inset we show (on a linear scale) the total atom populations in the low-k 'source' region $k_r < k_m$ and in the range $k_m < k_r < k_M$, where the power-law distribution is established in steady state (k_m and k_M are boundaries defined in the lower inset of Fig. 3a). Initially there is a net transfer of population from the source to the cascade region. The population growth in the cascade region means that the population flux through this k-space range is not constant at these early times. However, once the steady state is established, the population in the cascade k range saturates at a constant value, while the source is still slowly depleted. This is indeed what is expected for a direct cascade, in which a constant, k-independent population flux passes from the source, through the cascade range, to the high-k sink; formally, this population flux, for a given energy flux, should tend to zero as the sink is moved towards infinite energy[28]. (For a non-infinite-energy sink, one strictly speaking has a quasi-steady state, because at very long times the source would be too depleted to support a constant-flux cascade.)

We further cross-validate our experiments and first-principles calculations by fitting the cascade exponent γ in the range $k_m < k_r < k_M$. In Fig. 3c we show that, for $\Delta U/\mu \approx 1$, the experiment and simulations exhibit very similar evolution with the shaking time, and reach a steady-state value of γ after $t_s \approx 2$ s. In Fig. 3d we plot the measured and simulated γ values versus the shaking amplitude for fixed $t_s = 4$ s. Here we see that the steady-state value of γ is essentially independent of ΔU, reinforcing the robustness of our conclusions (for small ΔU the steady state is not reached for $t_s = 4$ s; see also the inset of Fig. 2e).

We lastly discuss our findings in the context of previous theoretical work. The γ we observe in both the experiment and simulations is close to one of the scarce analytical predictions—the Kolmogorov–Zakharov direct-cascade exponent $\gamma = 3$, for the weak-wave turbulence of a

compressible superfluid[28]. (This result is distinct from the prediction[1,2] for the Kolmogorov energy spectrum of incompressible-flow-dominated turbulence, $\mathcal{E}(k) \propto k^{-5/3}$.) This prediction is based on an idealized theory that starts with the GPE, but neglects the role of vortices and assumes weak interactions between the waves. Our simulations show that vortices are present in the system, but the value of γ suggests that they do not play a quantitatively important part in the turbulent cascade (observed at wavenumbers $k\xi \gtrsim 1$), and the Kolmogorov–Zakharov theory is a reasonable approximation. Consistent with this, in simulations we find that, in the relevant k range, the compressible-flow contribution to the energy dominates over that of the incompressible flow (see Methods, Extended Data Fig. 2). The small difference between $\gamma = 3.5$ and the approximate $\gamma = 3$ could arise as a result of several (interlinked) factors, such as a residual role of vortices, the non-negligible incompressible-flow energy, the fact that in reality the interactions between the waves are not necessarily weak[15,28], and the increasing importance of quantum pressure in the GPE with increasing k. The experimental flexibility offered by atomic gases, in particular the possibility to tune the strength of nonlinearity via Feshbach resonances, might enable better understanding of the applicability of the approximate analytical predictions, and the limitations of the classical-field methods.

Online Content Methods, along with any additional Extended Data display items and Source Data, are available in the online version of the paper; references unique to these sections appear only in the online paper.

Received 21 February; accepted 10 September 2016.

1. Kolmogorov, A. N. The local structure of turbulence in incompressible viscous fluid for very large Reynolds numbers. *Dokl. Akad. Nauk SSSR* **30,** 299–303 (1941).
2. Obukhov, A. On the distribution of energy in the spectrum of turbulent flow. *Dokl. Akad. Nauk SSSR* **32,** 22–24 (1941).
3. Sorriso-Valvo, L. *et al.* Observation of inertial energy cascade in interplanetary space plasma. *Phys. Rev. Lett.* **99,** 115001 (2007).
4. Mösta, P. *et al.* A large-scale dynamo and magnetoturbulence in rapidly rotating core-collapse supernovae. *Nature* **528,** 376–379 (2015).
5. Hwang, P. A., Wang, D. W., Walsh, E. J., Krabill, W. B. & Swift, R. N. Airborne measurements of the wavenumber spectra of ocean surface waves. Part I: spectral slope and dimensionless spectral coefficient. *J. Phys. Oceanogr.* **30,** 2753–2767 (2000).
6. Ghashghaie, S., Breymann, W., Peinke, J., Talkner, P. & Dodge, Y. Turbulent cascades in foreign exchange markets. *Nature* **381,** 767–770 (1996).
7. Gaunt, A. L., Schmidutz, T. F., Gotlibovych, I., Smith, R. P. & Hadzibabic, Z. Bose-Einstein condensation of atoms in a uniform potential. *Phys. Rev. Lett.* **110,** 200406 (2013).
8. Paoletti, M. S. & Lathrop, D. P. Quantum turbulence. *Annu. Rev. Condens. Matter Phys.* **2,** 213–234 (2011).
9. Chesler, P. M., Liu, H. & Adams, A. Holographic vortex liquids and superfluid turbulence. *Science* **341,** 368–372 (2013).
10. Maurer, J. & Tabeling, P. Local investigation of superfluid turbulence. *Europhys. Lett.* **43,** 29–34 (1998).
11. Walmsley, P. M. & Golov, A. I. Quantum and quasiclassical types of superfluid turbulence. *Phys. Rev. Lett.* **100,** 245301 (2008).
12. Bradley, D. *et al.* Direct measurement of the energy dissipated by quantum turbulence. *Nat. Phys.* **7,** 473–476 (2011).
13. Ganshin, A. N., Efimov, V. B., Kolmakov, G. V., Mezhov-Deglin, L. P. & McClintock, P. V. E. Observation of an inverse energy cascade in developed acoustic turbulence in superfluid helium. *Phys. Rev. Lett.* **101,** 065303 (2008).
14. Abdurakhimov, L. V., Brazhnikov, M. Y., Levchenko, A. A., Remizov, I. & Filatov, S. Turbulent capillary cascade near the edge of the inertial range on the surface of a quantum liquid. *JETP Lett.* **95,** 670–679 (2012).
15. Kolmakov, G. V., McClintock, P. V. E. & Nazarenko, S. V. Wave turbulence in quantum fluids. *Proc. Natl Acad. Sci. USA* **111,** 4727–4734 (2014).
16. Kagan, Y. & Svistunov, B. V. Evolution of correlation properties and appearance of broken symmetry in the process of Bose–Einstein condensation. *Phys. Rev. Lett.* **79,** 3331–3334 (1997); erratum **80,** 892 (1998).
17. Nore, C., Abid, M. & Brachet, M. E. Kolmogorov turbulence in low-temperature superflows. *Phys. Rev. Lett.* **78,** 3896–3899 (1997).
18. Berloff, N. G. & Svistunov, B. V. Scenario of strongly nonequilibrated Bose–Einstein condensation. *Phys. Rev. A* **66,** 013603 (2002).
19. Kobayashi, M. & Tsubota, M. Kolmogorov spectrum of superfluid turbulence: numerical analysis of the Gross–Pitaevskii equation with a small-scale dissipation. *Phys. Rev. Lett.* **94,** 065302 (2005).
20. Proment, D., Nazarenko, S. & Onorato, M. Quantum turbulence cascades in the Gross-Pitaevskii model. *Phys. Rev. A* **80,** 051603 (2009).
21. Reeves, M. T., Billam, T. P., Anderson, B. P. & Bradley, A. S. Inverse energy cascade in forced two-dimensional quantum turbulence. *Phys. Rev. Lett.* **110,** 104501 (2013).
22. Henn, E. A. L., Seman, J. A., Roati, G., Magalhães, K. M. F. & Bagnato, V. S. Emergence of turbulence in an oscillating Bose–Einstein condensate. *Phys. Rev. Lett.* **103,** 045301 (2009).
23. Neely, T. W. *et al.* Characteristics of two-dimensional quantum turbulence in a compressible superfluid. *Phys. Rev. Lett.* **111,** 235301 (2013).
24. Kwon, W. J., Moon, G., Choi, J., Seo, S. W. & Shin, Y. Relaxation of superfluid turbulence in highly oblate Bose-Einstein condensates. *Phys. Rev. A* **90,** 063627 (2014).
25. Tsatsos, M. C. *et al.* Quantum turbulence in trapped atomic Bose-Einstein condensates. *Phys. Rep.* **622,** 1–52 (2016).
26. Gotlibovych, I. *et al.* Observing properties of an interacting homogeneous Bose–Einstein condensate: Heisenberg-limited momentum spread, interaction energy, and free-expansion dynamics. *Phys. Rev. A* **89,** 061604 (2014).
27. Schmidutz, T. F. *et al.* Quantum Joule–Thomson effect in a saturated homogeneous Bose gas. *Phys. Rev. Lett.* **112,** 040403 (2014).
28. Zakharov, V. E., L'Vov, V. S. & Falkovich, G. *Kolmogorov Spectra of Turbulence* (Springer, 1992).

Acknowledgements We thank G. V. Shlyapnikov, B. Svistunov, S. Stringari, N. R. Cooper, J. Dalibard, M. J. Davis, R. J. Fletcher, M. W. Zwierlein, K. Fujimoto and M. Tsubota for discussions, and C. Eigen for experimental assistance. This work was supported by AFOSR, ARO, DARPA OLE, EPSRC (Grant No. EP/N011759/1) and ERC (QBox). The GeForce GTX TITAN X used for the numerical simulations was donated by the NVIDIA Corporation. N.N. and A.L.G. acknowledge support from Trinity College, Cambridge; R.P.S. acknowledges support from the Royal Society.

Author Contributions N.N. initiated the project, and took and analysed the data. A.L.G. wrote the code for the numerical simulations and analysed the results. Z.H. supervised the project. All authors contributed extensively to the interpretation of the data and the writing of the manuscript.

Author Information Reprints and permissions information is available at www.nature.com/reprints. The authors declare no competing financial interests. Readers are welcome to comment on the online version of the paper. Correspondence and requests for materials should be addressed to N.N. (nn270@cam.ac.uk).

METHODS

Experimental system. The BEC of ^{87}Rb atoms is produced in a quasi-uniform potential of a can-shaped dark optical dipole trap (see Fig. 1). The repulsive trap walls are sculpted using 532-nm laser light and a phase-imprinting spatial light modulator. They are formed by one circular tube beam (propagating along z) and two thin sheet beams that act as end caps[7]. At the end of evaporative cooling the trap depth is approximately $k_B \times 10\,\mathrm{nK}$ and the condensed fraction is $\eta > 0.9$. We then slowly (over 700 ms) raise the trap depth to $U_0 \approx k_B \times 60\,\mathrm{nK}$, which does not result in any observable drop in η. Our atom number is calibrated to within 10% from the critical temperature for condensation[27]. The gradient of the modulus of the magnetic field along z, used to shake the cloud, is calibrated by pulsing it on for a short time δt just after releasing the cloud from the trap and measuring the resulting velocity kick $\Delta U \delta t/(mL)$ in TOF.

Phase-shift measurement of the resonance. The position of the centre of mass of the cloud in TOF is vt_{TOF}, where v is its velocity at the time of release. In analogy with a driven damped harmonic oscillator, we assume that for a driving force proportional to $\sin(\omega t)$ in steady state $v(t) = A_\omega \omega \cos(\omega t + \phi_\omega)$, where A_ω and ϕ_ω are the ω-dependent (in-trap) displacement amplitude and phase shift. For a shaking time t_s such that ωt_s is a multiple of 2π, the response $v(t_s) = A_\omega \omega \cos(\phi_\omega)$ vanishes on resonance, and more generally

$$v(t_s) \propto \frac{\omega(\omega^2 - \omega_{\mathrm{res}}^2)}{(\omega^2 - \omega_{\mathrm{res}}^2)^2 + \Gamma^2\omega^2} \tag{1}$$

where Γ is the damping rate. In practice we fix $t_s = 2\,\mathrm{s}$ and make measurements at discrete points $\omega = j\Delta\omega$, where $\Delta\omega = 2\pi \times 0.5\,\mathrm{Hz}$ and j is an integer. We then use Equation (1) to fit the data (see Fig. 2b, d) with ω_{res} and Γ as free parameters.

Numerical methods. We implement a three-dimensional numerical simulation of the Gross–Pitaevskii equation (GPE)

$$i\hbar\frac{\partial\psi}{\partial t} = \left(-\frac{\hbar^2}{2m}\nabla^2 + V_{\mathrm{ext}}(\boldsymbol{r}, t) + g|\psi|^2\right)\psi \tag{2}$$

where the coupling constant is $g = 4\pi\hbar^2 a_s/m$, with a_s the s-wave scattering length, and $V_{\mathrm{ext}}(\boldsymbol{r}, t)$ is an external potential. We have $V_{\mathrm{ext}}(\boldsymbol{r}, t) = V_{\mathrm{box}}(\boldsymbol{r}) + V_s(\boldsymbol{r}, t)$, where $V_{\mathrm{box}}(\boldsymbol{r})$ is the (static) box-trap potential and $V_s(\boldsymbol{r}, t) = \Delta U \sin(\omega t) z/L$ is the (time-varying) shaking potential. We perform numerical simulations on a cubic grid of 256^3 points. Using a symmetrized split-step Fourier method we evolve the Bose field in time steps of 10 μs for up to 4 s. The calculations are performed at FP32 precision on an NVIDIA GeForce GTX TITAN X graphics card, and we achieve a running time of under 30 min for simulating each 1 s of dynamics.

Bogoliubov equations for the box trap. The starting point for the analysis of the linear response of the BEC to external perturbations is the GPE in Equation (2). We start by expanding $\psi(\boldsymbol{r}, t)$ around $\psi_0(\boldsymbol{r})$, the ground state in the potential $V_{\mathrm{ext}}(\boldsymbol{r}, t) = V_{\mathrm{box}}(\boldsymbol{r})$:

$$\psi(\boldsymbol{r}, t) = \mathrm{e}^{-i\mu t/\hbar}[\psi_0(\boldsymbol{r}) + u(\boldsymbol{r})\mathrm{e}^{-i\omega t} - v^*(\boldsymbol{r})\mathrm{e}^{i\omega t}]$$

where the asterisk denotes the complex conjugate. Linearizing with respect to u and v leads to the Bogoliubov equations:

$$\begin{pmatrix} \mathcal{L} & -gn_0 \\ gn_0 & -\mathcal{L} \end{pmatrix}\begin{pmatrix} u \\ v \end{pmatrix} = \hbar\omega\begin{pmatrix} u \\ v \end{pmatrix} \tag{3}$$

where

$$\mathcal{L} = -\frac{\hbar^2}{2m}\nabla^2 + V_{\mathrm{box}}(\boldsymbol{r}) - \mu + 2gn_0(\boldsymbol{r})$$

and $n_0(\boldsymbol{r}) = |\psi_0(\boldsymbol{r})|^2$ is the ground-state density. The set of eigenvalues $\hbar\omega$ forms the spectrum of elementary excitations, and u and v give the corresponding eigenmodes. For periodic boundary conditions, n_0 is constant and the usual Bogoliubov spectrum is recovered[29]. However, for fixed boundary conditions, the GPE cannot be solved analytically and $n_0(\boldsymbol{r})$ cannot be written in a simple closed form (it is not even separable in cylindrical coordinates). We solve the Bogoliubov equations by first computing $n_0(\boldsymbol{r})$ from an imaginary-time propagation of the GPE, and then numerically solving Equation (3). It is convenient to work in the basis of the free-particle eigenstates in a cylindrical box, so that the boundary conditions are automatically satisfied. Because we focus on the longitudinal modes, we restrict the basis to azimuthally symmetric functions. Our results for the frequency of the lowest-lying (antisymmetric) mode along z are shown in Fig. 2c as a grey shaded area (taking into account the uncertainty in the box size). In the limit of vanishing shaking amplitude, direct GPE simulations give the same results as the Bogoliubov approach.

Anisotropy analysis. To quantify the anisotropy of the TOF expansion, seen in the atomic distribution after a long t_{TOF}, we start with the column-density distribution in the TOF image $\tilde{n}(y, z) = \int n(\boldsymbol{r})\mathrm{d}x$, where $n(\boldsymbol{r})$ is the three-dimensional distribution and x is the imaging axis. We then define the angular density distribution:

$$p(\theta) = \frac{1}{\overline{N}}\int_{r_1}^{r_2} \tilde{n}(r\cos\theta, r\sin\theta) r\mathrm{d}r \tag{4}$$

where the polar origin is set at the centre of mass of $\tilde{n}(y, z)$ and $\overline{N}$ is the total atom number in the shell $[r_1, r_2]$, so that $\int_0^{2\pi} p(\theta)\mathrm{d}\theta = 1$. An isotropic distribution corresponds to the uniform $p_{\mathrm{iso}}(\theta) = (2\pi)^{-1}$. To quantify the anisotropy as a deviation from this uniform distribution, we introduce a simple heuristic measure:

$$\mathcal{A} = \frac{1}{2}\int_0^{2\pi}\left|p(\theta) - \frac{1}{2\pi}\right|\mathrm{d}\theta$$

so that $\mathcal{A} = 0$ for p_{iso} and $\mathcal{A} \to 1$ for sharply-peaked distributions. For our pure BEC, the diamond-shaped TOF distribution is close to the idealized square-shaped distribution depicted in the insets of Fig. 1b, d, for which (taking $r_1 = 0$ and $r_2 \to \infty$) the angular distribution is $p(\theta) = p_0(\theta \bmod \pi/2)$, with

$$p_0(\theta) = \frac{1}{8}\begin{cases} \cos^{-2}\theta & \text{for } 0 \le \theta < \pi/4 \\ \sin^{-2}\theta & \text{for } \pi/4 \le \theta < \pi/2 \end{cases}$$

For this distribution, $\mathcal{A} \approx 9\%$. In experiments, any imaging imperfections lead to a positive $\mathcal{A}$; for an equilibrium thermal gas ($\eta = 0$), which is known to be isotropic, we observe a small residual $\mathcal{A} \approx 3\%$, and define all our experimental values of $\mathcal{A}$ from this baseline. For the inset of Fig. 2e, the radial integration in Equation (4) is performed in the shell defined by $r_1 = \hbar k_{\mathrm{low}} t_{\mathrm{TOF}}/m$ and $r_2 = \hbar k_{\mathrm{high}} t_{\mathrm{TOF}}/m$ (corresponding to the vertical red lines in Fig. 3a).

Measurement of the momentum distribution. The measurement of the momentum distribution using the TOF technique requires a kinetic-energy-dominated state. We assess the validity of this measurement by comparing it to Bragg spectroscopy[30], which can provide a faithful measurement of the momentum distribution even if the interaction energy is dominant over the kinetic energy. We shine onto the trapped cloud two off-resonant laser beams with wavevectors $\boldsymbol{k}_1$ and $\boldsymbol{k}_2$, detuned from each other by a frequency $\Delta\nu$, such that the resultant 1D Bragg-diffraction optical lattice is aligned with the axis of the box trap, $\boldsymbol{k}_1 - \boldsymbol{k}_2 \propto \hat{\boldsymbol{z}}$. The angle between the beams is such that the recoil energy of the diffracted atoms $E_r \approx k_B \times 320\,\mathrm{nK}$ is larger than the trap depth ($U_0 \approx k_B \times 60\,\mathrm{nK}$), allowing the diffracted atoms to escape, and also much larger than the spread of energies in the trapped gas. Measuring the fraction of diffracted atoms as a function of $\Delta\nu$ yields the 1D momentum distribution along $\hat{\boldsymbol{z}}$, $n_{1\mathrm{D}}(k_z)$, which is related to the planar distribution $\tilde{n}$ (measured in TOF) by an Abel transform:

$$n_{1\mathrm{D}}(k_z) = \int_{-\infty}^{+\infty}\tilde{n}\left(\sqrt{k_y^2 + k_z^2}\right)\mathrm{d}k_y$$

We use a long (20 ms) and low-power Bragg pulse to minimize Fourier broadening while always keeping the diffracted fraction below 15%. To compare the TOF and Bragg measurements we integrate our TOF images along $\hat{\boldsymbol{y}}$.

In Extended Data Fig. 1a, we apply both methods to the initial state, a quasi-pure BEC. In this case the TOF measurement (solid green line) overestimates the width of the momentum distribution, owing to the importance of interactions during the expansion; the Bragg spectrum agrees well with the expected Heisenberg-limited distribution (dashed red line)[26]. However, as shown in Extended Data Fig. 1b, in the relevant case of the kinetic-energy-dominated turbulent state, the Bragg and TOF measurements are in excellent agreement, validating our assumptions.

Background-gas losses. In the absence of shaking, the atom population in the trap slowly decays owing to collisions with the residual background gas in the vacuum chamber. These one-body losses are k-independent and described by an exponential decay with a time constant that we measured to be $\tau_{\mathrm{vac}} = 13\,\mathrm{s}$. For analysing the population dynamics in the inset of Fig. 3b, we corrected all populations for this background loss by multiplying them by a common factor $\exp(t_s/\tau_{\mathrm{vac}})$.

Numerical simulations of the turbulent cascade. In Extended Data Fig. 2a we show simulations of the dynamics of the in-plane momentum distribution in a shaken gas. Here $\tilde{n}(k)$ is computed from the spatial Fourier transform of the matter-wave field $\psi(\boldsymbol{r}, t_s)$. We observe that with increasing t_s the same power-law behaviour gradually extends from large to ever smaller length scales, as expected for a direct cascade.

Following the procedure outlined in ref. 17, we also study the fluid-dynamical kinetic-energy spectrum $\mathcal{E}(k)$. We start by computing $\widetilde{\boldsymbol{w}}(\boldsymbol{k})$, the Fourier transform of the flow field

$$\boldsymbol{w}(\boldsymbol{r}) = (\hbar/m)|\psi(\boldsymbol{r})|\nabla\varphi(\boldsymbol{r})$$

where $\varphi(\boldsymbol{r})$ is the phase of $\psi(\boldsymbol{r})$ and we omit the time label for brevity. Summing $|\widetilde{\boldsymbol{w}}(\boldsymbol{k})|^2$ over all momenta with $|\boldsymbol{k}| = k$ gives the total $\mathcal{E}(k)$. Decomposing $\widetilde{\boldsymbol{w}}(\boldsymbol{k})$ into longitudinal and transverse components splits $\mathcal{E}(k)$ into the compressible- ($\mathcal{E}_c$) and incompressible-flow ($\mathcal{E}_i$) contributions, respectively. In Extended Data Fig. 2b we plot the ratio $\mathcal{E}_c(k)/\mathcal{E}_i(k)$. We find that $\mathcal{E}_c(k)$ dominates in the k range $k_m < k < k_M$, where the power-law momentum distribution is observed in both experiments and simulations; the same numerical observation was independently made by K. Fujimoto and M. Tsubota (personal communication). This supports the view that waves play a more important part than vortices in the turbulent cascade. Also, the vortices have a core size of approximately ξ, so it qualitatively makes sense that their contribution is not important when $k \gtrsim 1/\xi$.

Data availability. Source Data for Figs 1–3 and Extended Data Figs 1, 2 are available online.

29. Pitaevskii, L. P. & Stringari, S. *Bose–Einstein Condensation and Superfluidity* Ch. 12 (Oxford Univ. Press, 2016).
30. Stenger, J. *et al.* Bragg spectroscopy of a Bose–Einstein condensate. *Phys. Rev. Lett.* **82,** 4569–4573 (1999).

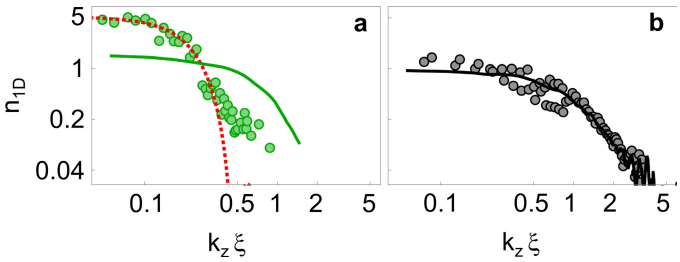

Extended Data Figure 1 | Momentum distributions from TOF and Bragg techniques. a, **b**, Comparison of $n_{1D}(k_z)$ obtained using TOF expansion (solid lines) and Bragg spectroscopy (points), in the case of the initial, quasi-pure BEC (**a**) and the turbulent gas (**b**). The red dashed line in **a** corresponds to the Heisenberg-limited momentum distribution. All distributions are normalized to unity ($\int_0^\infty n_{1D}\mathrm{d}(k_z\xi) = 1$), without any adjustable parameters.

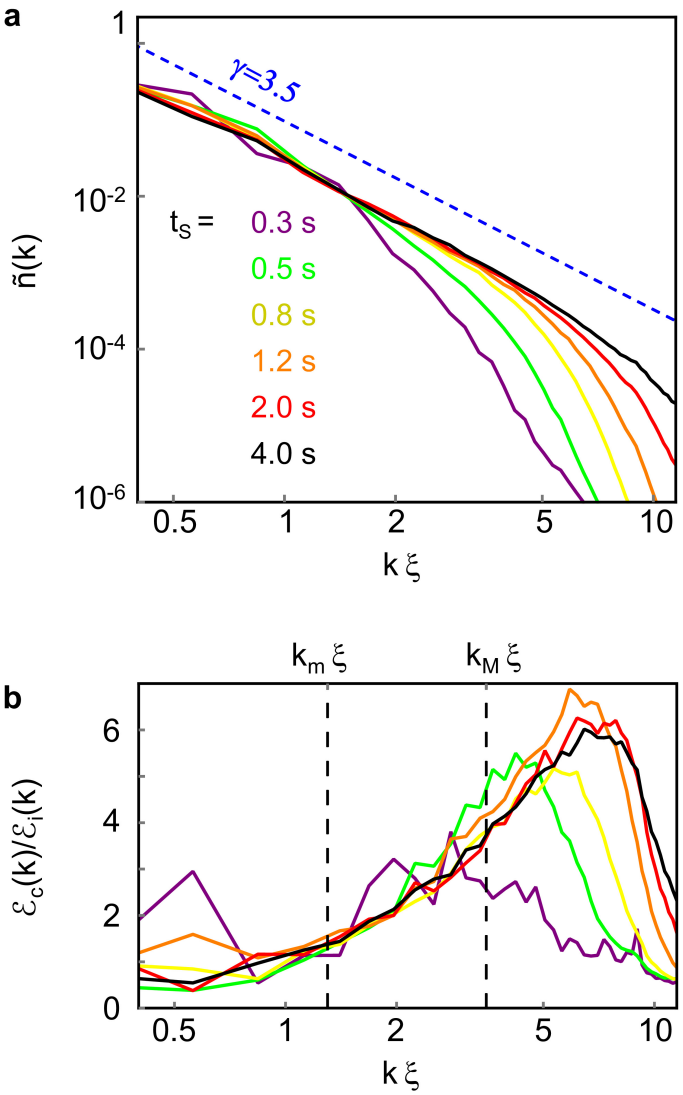

Extended Data Figure 2 | Turbulent cascade in numerical simulations. **a**, In-plane momentum distribution $\tilde{n}(k)$ for various shaking times t_s. **b**, Ratio of the compressible- ($\mathcal{E}_c$) to incompressible-flow ($\mathcal{E}_i$) components of the fluid-dynamical kinetic energy, with the colours corresponding to the shaking times in **a**. The simulation parameters for both panels are $N = 8 \times 10^4$, shaking frequency $\omega/(2\pi) = 9$ Hz and shaking amplitude $\Delta U = \mu$.